Operando analysis of the electrosynthesis of Ag2O nanocubes by scanning electrochemical microscopy

Mathias Miranda Vieira, Jean-François Lemineur, Jérôme Médard, Catherine Combellas, Frédéric Kanoufi, Jean-Marc Noël

Operando analysis of Ag_2O nanocubes electrosynthesis by scanning electrochemical microscopy

Mathias Miranda Vieira, Jean-François Lemineur, Jérôme Médard, Catherine Combellas, Frédéric Kanoufi[*], Jean-Marc Noël[*]

Université de Paris, ITODYS, CNRS, F-75006 Paris, France

[*]Corresponding authors:
jean-marc.noel@u-paris.fr
frederic.kanoufi@u-paris.fr

Keywords: nanoparticles, metal oxides, scanning electrochemical microscope, Electrochemical-impacts, single entity electrochemistry, electrosynthesis.

Abstract

The strategy proposed herein employs the scanning electrochemical microscope in a generation collection like mode to depict the mechanism implied in the electrosynthesis of metal oxides nanoparticles, NPs. It offers a simultaneous generation of the NPs precursors and a single NP-level electroanalysis by nanoimpact coulometry. The former process is operated under controlled fluxes within the wide field of precursor diffusion in the inter-MEs gap thus forming a tunable reaction layer allowing the growth of NPs size gradient within this gap. The latter process exploits the much slower diffusion of NPs, spatially frozen, in the near field of a collecting microelectrode. It then allows to dynamically and *in situ* monitor the modes of growth of NPs without perturbing their synthesis. As a proof of concept, the synthesis of Ag_2O nanocubes, NCs, is described, using an Ag microelectrode to generate Ag^+ ions while a facing Au microelectrode both electrogenerates HO^- and collect the as-synthetized Ag_2O NCs. The dynamic analysis of the NCs reductive electrochemical impacts, allows getting insights in their growth and stability. Particularly it suggests a two steps growth mechanism starting from a quasi-instantaneous nucleation of a >260 nm nucleus followed by a mass-transfer driven crystallization over the nuclei.

1 Introduction

Metal oxides nanoparticles (MeOx NPs) are used in many applications ranging from bio- and nano-medicine, optics, electronics, electrocatalysis, or sensing [1,2]. Different synthetic routes are now available, allowing to get highly mono-disperse MeOx NPs with well controlled size and geometry [3,4]. However, most of the existing studies to control their synthesis rely on trials and errors, which is time and cost consuming. Therefore, it appears relevant to elaborate *operando* strategies allowing a fast screening of the experimental conditions for the MeOx NPs synthesis and their characterization during their formation.

In this respect, electrochemical strategies are particularly promising. On the one hand, one can design electrosynthetic routes in which an electrode delivers at controlled fluxes the NP synthetic precursors, thus enabling a rapid screening of many experimental parameters [5]. MeOx NPs can be electrosynthesized by employing a sacrificial anode as a metallic precursor source, frequently facing a second electrode used to increase the pH of the solution, for example by triggering the water splitting reaction [6].

On the other hand, single entity electrochemistry provides a high temporal resolution operando characterization of NPs. It was used to monitor *operando* the formation of metallic [7], multi-metallic [8], metal organic framework [9], inorganic material [10], and core shell NPs [11,12]. Meanwhile, the electrochemical nanoimpacts strategy, relying on the analysis of the current fluctuations associated with the reaction of single NPs with a polarized micro- to nano-sized interface, is now a mature electrochemical method for detecting and characterizing NPs in solution. The predominant strategies usually employ the catalytic amplification of current by NPs at an electrode [13], or a liquid/liquid interface [14], the partial hindrance by NPs of the electrode diffusion layer [15,16], or the coulometry of the direct transformation of NPs at an electrode [17–19].

Herein, both synthetic and analytical strategies are combined to inspect MeOx NPs synthesis. For this purpose, the scanning electrochemical microscope (SECM) [20] is employed in a generation/collection-like configuration allowing the simultaneous electrochemical generation and collection of MeOx NPs, a configuration close to that used to collect Ag^+ ions released from the oxidative nanoimpact of Ag NPs [21]. As a proof of concept, the nucleation and growth of silver oxide nanocubes (Ag_2O NCs), known to be synthesizable electrochemically [22], is studied, owing to their interest as antimicrobials [23], in rechargeable alkaline batteries [24] or photo-catalysis [25].

2 Materials and Methods

2.1 Chemicals and Materials

Potassium nitrate (KNO_3) and sulfuric acid (H_2SO_4 95%) were obtained from Prolabo and VWR respectively. All solutions were prepared using ultrapure water (resistivity > 18.2 MΩ.cm). Ultramicroelectrodes (UMEs) were fabricated using 25 µm diameter Ag wires (99.99%, Goodfellow Cambridge Ltd), sealed in 1.0 mm/0.5 mm (outer/inner diameter) borosilicate glass capillaries (Sutter Instruments) using a P2000 laser puller (Sutter Instruments). Before use, the UMEs were polished on aluminum oxide tape (3 µm, Precision Surfaces International, Houston, Texas), washed with ultra-pure water and technical grade ethanol and then sonicated whereas a homemade 500 µm diameter Au microelectrode (ME) was cleaned by electrochemical restructuration by cycling between -0.8 and 1.4 V vs Ag QRCE for 5 min in a H_2SO_4 50 mM solution.

2.2 Scanning electron microscopy (SEM)

SEM images were recorded with a SEM-FEG SUPRA 40 from Zeiss.

2.3 SECM experiments

A CHI-910B (CH-Instruments) was used in a Faraday cage to perform the SECM experiments with a bipotentiostat in a 3-electrode configuration and a 1mm diameter silver wire as a quasi-reference/counter (QRCE) electrode. The distance between the Ag UME and the Au Me was evaluated from approach curves [20] by applying -1.0 V at the Ag UME to trigger the hydrogen evolution reaction. The methodology consists in retracting the UME (Rg ~ 10) of 150 µm after it has touched the generator surface. The physical contact is attested when a current plateau is reached on the approach curves. The electrochemical impact transients were acquired at a frequency of 250 Hz and were analyzed by a homemade Matlab routine in which events detection corresponds to a signal-to-noise ratio higher than 5.

3 Results and discussion

3.1 *Principle of Ag_2O NCs electrosynthesis and SEM characterization*

Ag_2O NCs are electrosynthesized in a 0.1 M KNO_3 aqueous solution from two working electrodes facing each other and separated by 150 µm as illustrated in Figure 1a. In this configuration, a 25 µm diameter Ag sacrificial UME is used to produce Ag^+ precursor through the application of a sufficiently anodic potential (1). Meanwhile, the facing Au 500 µm ME is biased at a cathodic potential promoting the oxygen reduction reaction (ORR), leading to the formation of HO^- via a 2 to 4-electron transfer (2a-2b) [26] and consequently a local pH increase. The precipitation of HO^- and Ag^+ generates colloidal Ag_2O NCs in the inter-ME gap (3). Simultaneously, the generated Ag_2O NCs can be collected at the Au ME by (4) their reductive electrochemical (EC) impacts conversion into Ag (Figure 1a).

$$Ag \rightarrow Ag^+ + e^- \quad (1)$$

$$O_2 + 2H_2O + 4e^- \rightarrow 4HO^- \quad (2a)$$

$$O_2 + 2H_2O + 2e- \rightarrow H_2O_2 + 2HO^- \quad (2b)$$

$$2Ag^+ + 2HO^- \rightarrow Ag_2O + H_2O \quad (3)$$

$$Ag_2O + H_2O + 2e^- \rightarrow 2Ag + 2HO^- \quad (4)$$

A typical SECM experiment consists in recording current-time transients simultaneously at the Au ME and Ag UME while triggering respectively the ORR (E_{Au} = -0.4 V determined from cyclic voltammetry, CV, shown in Figure SI1 of the supplementary information) and the release of Ag^+ (E_{Ag} =+ 0.3 V). The typical EC responses recorded at both MEs are shown in Figure 1b. The CA at the Au ME (bottom of Figure 1b) shows stochastic reductive current spikes > 50s after the onset of the experiment. An example of the current spike zoomed is shown in Figure SI2. These spikes, characteristic of EC impact events [17,18], are attributed to the reduction of Ag_2O NCs. In such experimental configuration, the Au ME then acts simultaneously as a HO^- source and as a NCs collector. A NC edge length, a_{NC}, was inferred from the charge of each current spike, Q, assuming a complete 2-electron reduction of the Ag_2O NCs which was already evidenced during the electrochemical reduction of AgX NPs [18,27,28]:

$$a_{NC,m} = \sqrt[3]{\frac{QV_{m,Ag2O}}{2F}} \quad (5)$$

where F is the Faraday constant and $V_{m,Ag2O} \approx 33$ cm^3/mol is the molar volume of Ag_2O. The ensemble spikes provides a distribution NC size shown in Figure 1c, is centered at $a_{NC,m}$ ~ 400-nm.

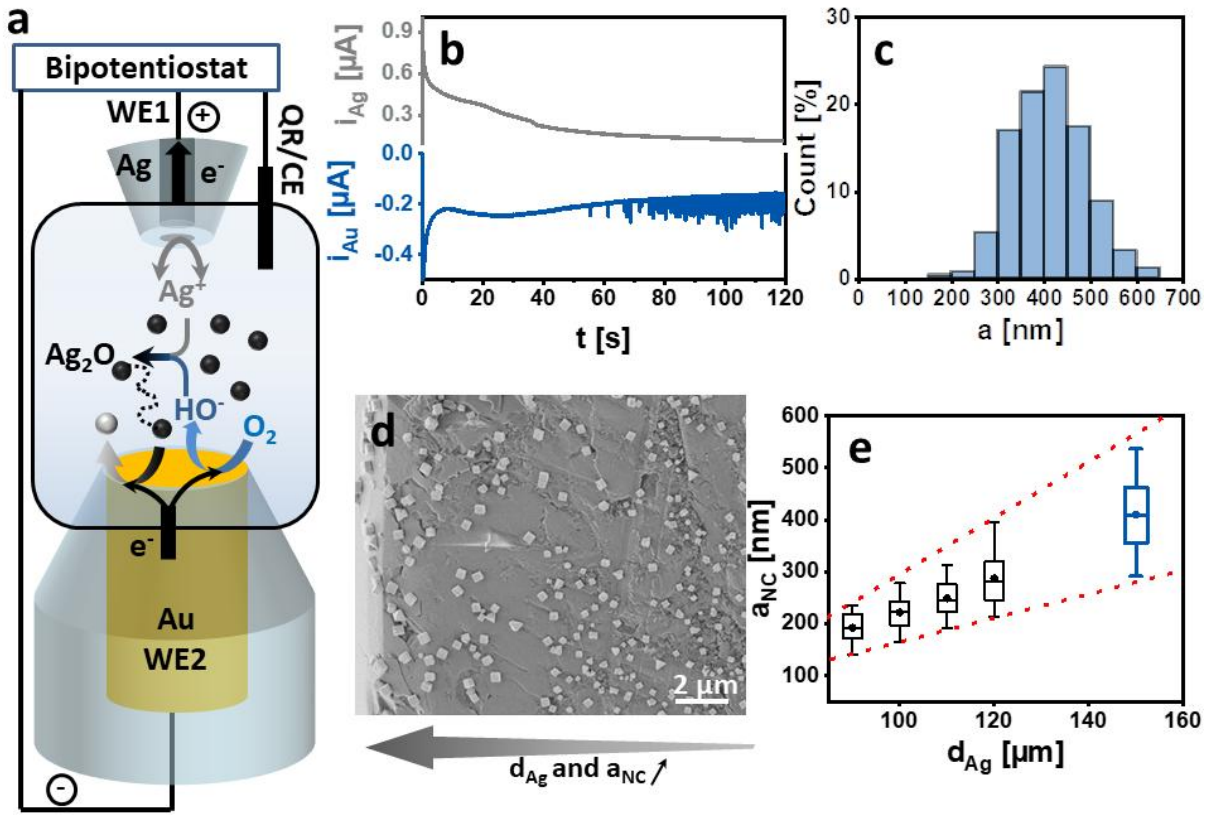

Figure 1. (a) Schematic representation of the generation/collection like SECM mode to study the Ag_2O NCs electrosynthesis. (b) CA experiments using a 25 µm diameter Ag UME facing a 500 µm diameter Au ME separated by d ~ 150 µm and by applying E_{Ag} = +0.3 V and E_{Au} = -0.4 V. (c) Corresponding NCs edge length distribution histogram. d) Subsequent SEM imaging of the glass part of the Ag UME showing the evolution of the NCs size. (e) Box plot of the NCs edge length as a function of the distance from the Ag wire extracted from (black) the SEM images in (d) and (blue) the NCs edge length distribution in (c).

Subsequently, the NPs were characterized by *ex situ* SEM imaging recorded on the glass part of the apex of the Ag UME after the CA. The SEM images evidence the presence of NCs whose average size depends on the distance from the center of the UME, as shown in Figure 1d. The NCs size was deeply analyzed at various distances from the Ag UME following the procedure described in Figure SI3. The box plots of a_{NC} for distances between 90 µm to 120 µm from the Ag wire highlight an increase from a_{NC} ~ 180±50 nm at 90±5 µm to a_{NC} ~ 260±80 nm at 120±5 µm, as shown in Figure 1e. The evolution of a_{NC} with the distance to the UME center is attributed to the concentration gradient of the precursors generated at their respective electrodes (*i.e.* HO^- at Au ME and Ag^+ at Ag UME) modifying their concentration ratio in the reaction layer and eventually the NCs growth rate.

Interestingly, the NCs edge lengths extracted from the EC impact are larger than those obtained by the SEM. However, as seen in Figure 1e (blue box plot), this is within the range of values that can be expected for a 150 µm inter-ME gap by extrapolating the trend of the a_{NC} with the distance from the Ag wire observed by SEM.

Noteworthy, owing to their size distribution, the NCs collected have a distribution of diffusion coefficient D_{NC} given from the Stokes-Einstein relationship (6)

$$D_{NC} = \frac{k_B T}{6\pi\eta a_{NC}\sqrt[3]{\frac{3}{4\pi}}} \quad (6)$$

D_{NC} ~ 0.6 ± 0.2 µm^2/s with η = 0.89 mPa.s and $\sqrt[3]{\frac{3}{4\pi}}$ is the term considering the cubic shape of the NPs. During the t ~ 100 s duration of the CA the collected NCs have at best travelled by diffusion to the ME from $d_{coll} \sim \sqrt{D_{NC} t}$ < 10 µm. Therefore, since the NCs diffuse >3 orders of magnitudes more slowly than their ionic precursors, the collecting Au ME probes a limited sample within the NCs population (<10% considering their growth in all the area within the inter-ME gap according to the SEM), minimizing the perturbation of the NC synthesis.

3.2 Influence of the Ag^+ production rate studied by EC impact experiments

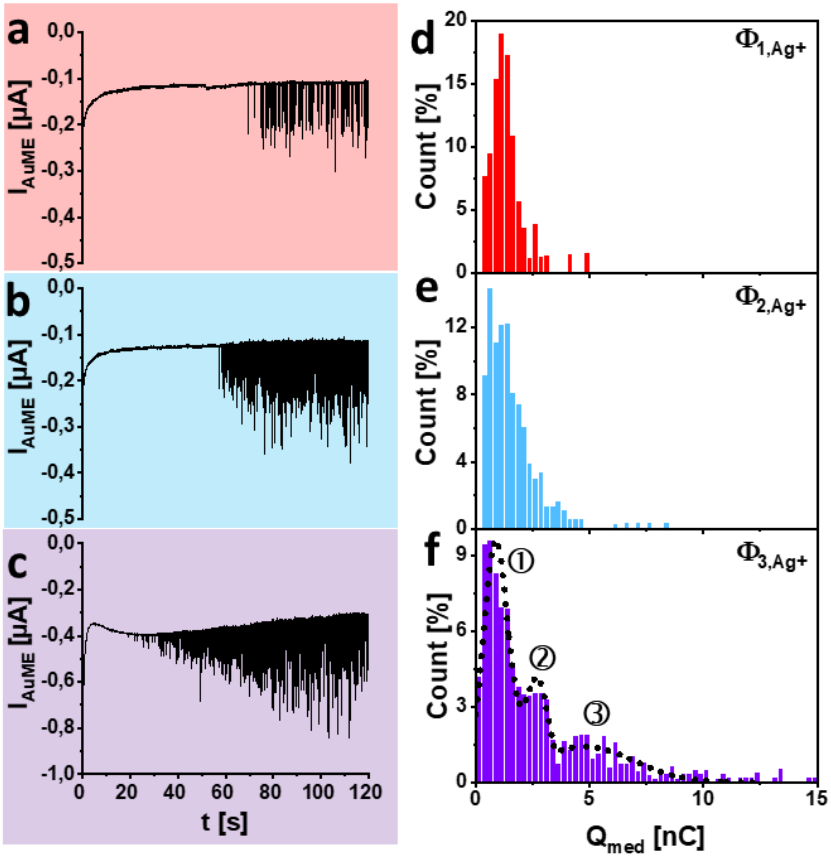

Figure 2. Current-time transients measured at the gold ME (E_{Au} = -0.4 V) for various Ag^+ production rates generated from a sacrificial 25 µm diameter Ag UME ($\phi_{1,Ag+} \approx 280$ fmol.s^{-1} (a), $\phi_{2,Ag+} \approx 530$ fmol.s^{-1} (b) and $\phi_{3,Ag+} \approx 3950$ fmol.s^{-1} (c)) and their corresponding peak charge distribution histogram (d), (e), (f) for $\phi_{1,Ag+}$, $\phi_{2,Ag+}$ and $\phi_{3,Ag+}$, respectively.

To further illustrate the relevance of our approach, the effect of the amount of precursors generated at the electrodes on the resulting Ag_2O NCs was studied. Only the concentration of Ag^+ is modulated here, but the same methodology can be employed to study the effect of HO^- concentration or the inter-ME gap. The production rate of Ag^+ ions electrogenerated at the Ag UME, ϕ_{Ag+}, is estimated from its steady-state current, i, according to

$$\phi_{Ag+} = \frac{i}{F} \quad (7)$$

from which the concentration $C^0_{Ag+} = \frac{\phi_{Ag}}{4D_{Ag}}$ at the UME is evaluated with D_{Ag} = 1.6.10^{-5} cm^2.s^{-1} the Ag^+ diffusion coefficient [29] and a_{Ag} = 12.5 µm the radius of the Ag part of the UME. Noteworthy, this production rate also provides an estimate of Ag^+ at distance r from the UME. By a first flux conservation approximation, Ag^+ is expected to expand hemispherically and

$$C_{Ag+}(r) \sim \frac{a}{r} C^0_{Ag+} = \frac{\phi_{Ag}}{4D_{Ag} r}. \quad (8)$$

Current transients were recorded at the Au ME by generating three different Ag^+ production rates at the Ag UME ($\phi_{1,Ag+} \approx 280$, $\phi_{2,Ag+} \approx 530$ and $\phi_{3,Ag+} \approx 3950$ fmol.s^{-1} extracted from the corresponding transients in Figure SI4 by applying $E_{1,Ag+}$ = 0.23V, $E_{2,Ag+}$ = 0.25V and $E_{3,Ag+}$ = 0.30 V respectively), while maintaining constant the current at the Au ME (E_{Au} = -0.4 V, i.e. a same rate of HO^- production $\phi_{HO^-} \approx 1100$ fmol.s^{-1} considering (7) extracted from Figure 2a or b). The transients are shown in Figure 2a, b and c, respectively. Noteworthy, the apparent current recorded at the AuME at high Ag^+ production rate is higher than at lower flux, which can be attributed to the direct electrodeposition of Ag^+ at the Au ME. The corresponding concentrations of Ag^+ can be estimated from equation 8 as $C_{1,Ag+}$ = 0.30, $C_{2,Ag+}$ = 0.55 and $C_{3,Ag+}$ = 4.1 mM with r = 150 µm and assuming their negligible consumption to form nanocubes, whereas C_{HO-} generated at the Au ME is within the 0.2 to 0.4 mM range considering either a 2 or a 4-electron reduction (equations 2a and 2b):

$$C_{HO-} = \frac{I}{4nFD_{O2}a_{Au}} \quad (9)$$

where a_{Au} = 250 µm is the radius of the Au part of the Au ME, D_{O2} = 2x10^{-5} cm^2.s^{-1} [30] and I ~ 0.13 µA the steady state current of Figure 2a and b.

Figure 2d, e and f provide the charge distributions extracted from the transients recorded for $\phi_{1,Ag+}$, $\phi_{2,Ag+}$ and $\phi_{3,Ag+}$ respectively. The charge distributions corresponding to $\phi_{1,Ag+}$ and $\phi_{2,Ag+}$ (Figures 2d and e) are similar, whereas the average impact frequency, f, traducing the number of NPs impacting the Au ME over time, and therefore the local NC concentration increases ($f_{1,Ag+} \approx 2.1$ Hz, $f_{2,Ag+} \approx 8.3$ Hz). It shows that doubling the Ag^+ production rate increases the NCs concentration without much changing their size, in the vicinity of the Au ME. However, as observed in Figure 2f, for >10 times increase of the Ag^+ production rate ($\phi_{3,Ag+}$), in addition to the increase of the NC concentration (impact frequency, $f_{3,Ag+} \approx 11.3$ Hz), the size distribution is also broadened. This distribution actually presents three populations of NCs, which were fitted by three Gaussians noted ①, ② and ③ in Figure 2f. Interestingly, the predominant population ①, is similar to the population observed at lower Ag^+ production rate $\phi_{1,Ag+}$ and $\phi_{2,Ag+}$, characterized by an equivalent median charge ($Q_{1,med}$ = 1.14 nC, $Q_{2,med}$ = 1.14 nC, $Q_{3,med①}$ = 1 nC for $\phi_{1,Ag+}$, $\phi_{2,Ag+}$ and $\phi_{3,Ag+}$ respectively). It suggests that the NCs median edge length is mainly independent of the Ag^+ production rate. On the other hand, the populations ② and ③ in Figure 2f most likely reflect the agglomeration of NCs of median edge length 0.7 and 1 µm respectively. It also suggests that the critical concentration needed to avoid the agglomeration is exceeded, revealing the importance of controlling the precursor concentration during the electro-synthesis of NPs in the absence of capping agent.

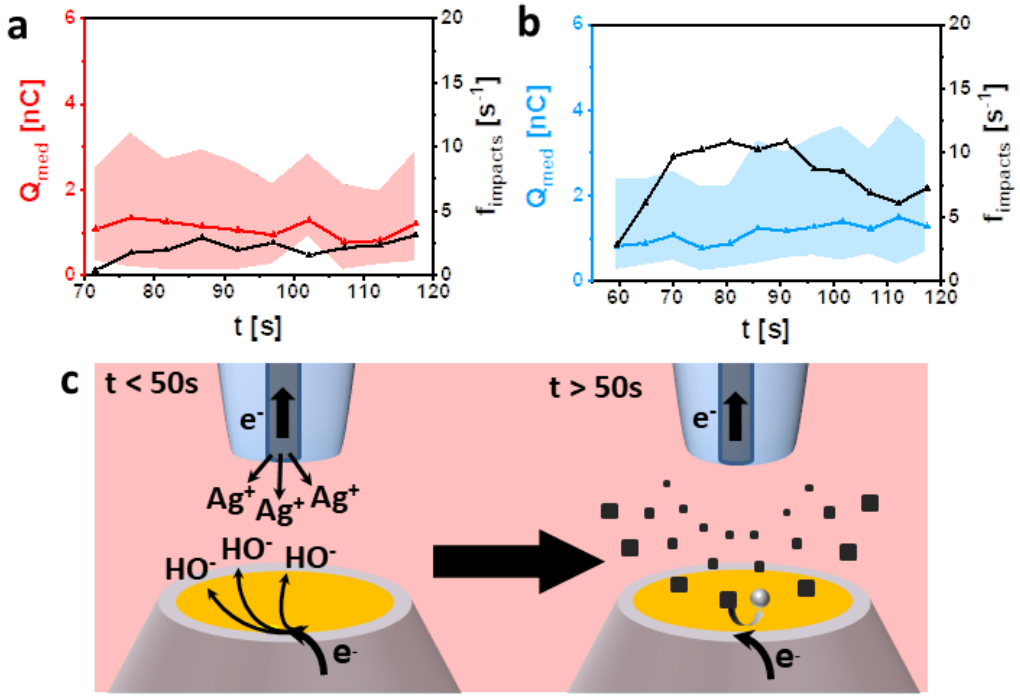

Figure 3. Median peak charge (Q_{med}) and frequency evolution as a function of time for (a) $\phi_{1,Ag+}$ and (b) $\phi_{2,Ag+}$. The shaded areas correspond to the 1st and 3rd quartiles of the median peak charge. c) Illustration of the instantaneous NCs formation/collection corresponding to $\phi_{1,Ag+}$ or $\phi_{2,Ag+}$.

A closer analysis of the Au ME current transients reveals a decrease of the time of the first impact with the Ag^+ production rate, from ~70 s in Figure 2a to ~50 s in Figure 2b and to < 20 s in Figure 2c. Noteworthy, this cannot be attributed to the limit of detection which for a SNR~2 would correspond to a current spike of 3nA amplitude and 10ms duration (the minimum duration extracted from the distributions in Figure SI5), i.e. a 15 pC charge for the reduction of a ~ 130 nm NC. The charge of the first impact detected in the transients of Figures 2a and b, 1.4 and 0.4 nC respectively are much larger than the LOD.

A further dynamic dissection of the transients of Figure 2a and Figure 2b was realized by repeating the charge and frequency analysis, but within a short time interval (Δt = 5 s) to study the evolution of both NCs edge lengths (charge) and their concentration (impact frequency) with time. The median charge and the first and third quartiles, as well as the frequency within Δt all along the transients were computed and are depicted in Figures 3a, b for $\phi_{1,Ag+}$ and $\phi_{2,Ag+}$ respectively. The average spike charge and the frequency remain mostly constant during the whole transient, suggesting that NCs are continuously produced at the same limited size and concentration from the onset of their detection. Typically, when they impact the Au ME they have a median size $a_{NC,med}$ ~ 550 nm. The collection of such large NCs is consistent with the SEM image in Figure 1d showing that the largest NCs are located farther from the Ag wire. This suggests instantaneous and limited NCs growth, at least compared to the characteristic electrochemical collection time. One can notice that < 1s growth of Ag_2O NPs of comparable size was evidenced previously [22]. Such fast growth could be possible if the concentration of Ag^+ and HO^- reach supersaturation conditions allowing to trigger the fast crystallization of Ag_2O as illustrated in Figure 3c. Indeed such a supersaturation condition is most likely as C_{Ag+} > 0.3mM at the Au UME meaning that the supersaturation $S = \frac{C_{HO-}\, C_{Ag+}}{Ks} > 5$ where Ks = 2x10^{-8} M^2 is the solubility product [31].

Considering such a mechanism, the delay between the beginning of the precursors generation and the collection of the NCs could correspond to the induction time, which can vary between 1 ms and 6000 s and is known to decrease with an increase of S [10,32]. This is qualitatively in line with the decrease of the time of first impact with the increase of S observed from $\phi_{1,Ag+}$ to $\phi_{3,Ag+}$.

For the highest Ag^+ production rate, a smaller NC, a_{NC} = 260 nm, is first detected in Figure 2c and the dynamic analysis in Figure 4a reveals that the median NC size increases with time from $a_{NC,med}$ ~ 300 nm at the first time-period Δt until it reaches, at longer times, $a_{NC,med}$ ~ 600 nm similar to the limiting sizes observed for the low production rate conditions (Figure 4c).

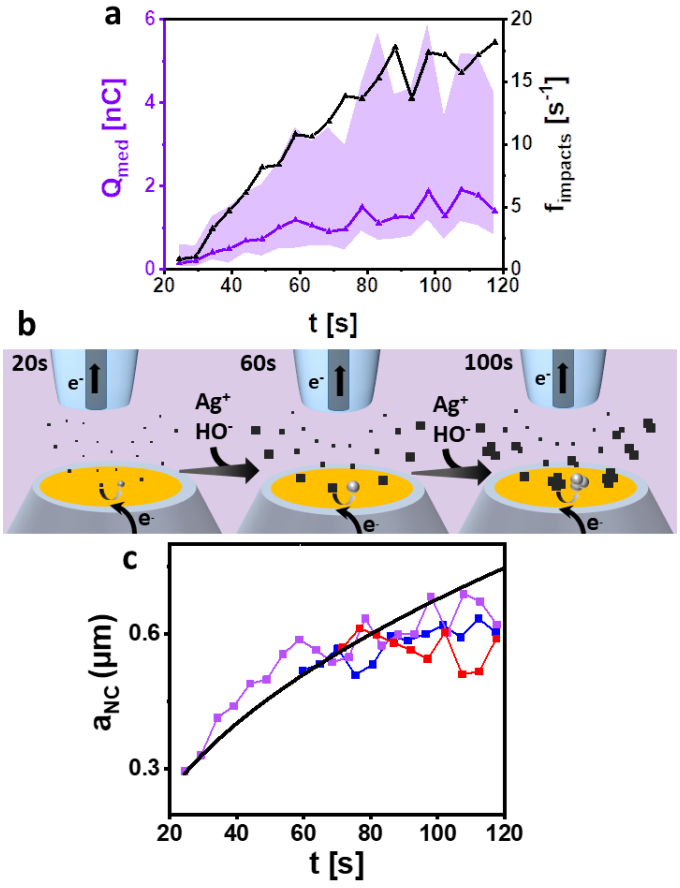

Figure 4. (a) Median peak charge (Q_{med}) and frequency evolution as a function of time for $\phi_{3,Ag+}$. The shaded areas correspond to the 1st and 3rd quartiles of the median peak charge. b) Mechanism of instantaneous formation/collection followed by overgrowth of NCs corresponding to $\phi_{3,Ag+}$. (c) Ag_2O NCs edge length extracted from Q_{med} for $\phi_{1,Ag+}$ (red), $\phi_{2,Ag+}$ (blue), $\phi_{3,Ag+}$ (purple) and the NCs growth theoretical fit (black) using κ = 0.02 µm^2.s^{-1}.

The formation of smaller NCs at higher concentration is consistent with the distance effect on the NC size: the closer from the Ag^+ source, the higher the Ag^+ concentration and the smaller the NC. It is indeed expected that higher precursor concentration (higher supersaturation or Ag^+ local concentration) could produce smaller NCs [33].

On the other hand, the frequency of impact, *f*, also increases steadily with the electrosynthesis time from 1Hz at the first instants to ca. 17 Hz 100s later, revealing a continuous generation of new NCs. Interestingly, populations ② and ③ of NCs pointed in Figure 2f actually appear

when the frequency f > 10 Hz suggesting that the agglomeration phenomenon starts above this limiting frequency as illustrated in Figure 4b.

Finally, apart from the aggregates formed, the continuous increase of the median NCs size is attributed to the continuous arrival of Ag^+ and HO^- precursors allowing to feed the existing NCs through an overgrowth mechanism (Figure 4b). The dynamics of such NCs overgrowth is dynamically probed here. Assuming that the NCs overgrowth is limited by the reactants mass transfer, an apparent overgrowth rate constant κ was assessed by fitting the evolution of $a_{NC,med}$ by:

$$a_{\mathrm{NC}}(t) = a_{\mathrm{NC},0}\sqrt{1 + \frac{\kappa}{2\pi(\sqrt[3]{\frac{3}{4\pi}}a_{\mathrm{NC},0})^2}(t - t_0)} \quad (10)$$

with $a_{\mathrm{NC},0}$ ~300 nm the initial NC size estimated at t_0 = 25 s.

As shown in Figure 4c, the best fit is obtained with κ = 0.02±0.01 $\mu m^2.s^{-1}$, a value close to those obtained recently during the optical monitoring of metallic Ag NCs growth [34,35].

4 Conclusion

The SECM in a generation/collection like mode is an interesting tool to explore the mechanisms of NPs electrosynthesis. It combines a simultaneous generation of the NPs precursors and a single NP-level electroanalysis by nanoimpact coulometry. The former process is operated under controlled fluxes within the wide field of precursor diffusion in the inter-MEs gap thus forming a tunable reaction layer allowing the growth of NPs having a size gradient within this gap. The latter process exploits the much slower diffusion of NPs, in the near field of the collecting ME allowing to probe a small fraction of the NCs (<10%) and synthetized close to it. The EC impact then allows to dynamically and *in situ* monitor the modes of growth of NPs without perturbation of their synthesis, while the SEM, as a complementary technique, provides a distance effect but at a given time. It is illustrated herein for the electrosynthesis of Ag_2O NCs through the analysis of the effect of Ag^+ precursor electrogenerated rate on their growth mode. It is shown that the NC formation proceeds by an instantaneous crystallization of unexpectedly large (>260nm) nuclei-NCs whose size or concentration is dictated by the Ag^+ local concentration, suggesting a growth controlled by a supersaturation mechanism. At higher Ag^+production rate, both the NCs size and concentration increase along the electrosynthesis time. The NC size increase is assigned to a mass-transfer driven crystallization over the nuclei-NCs. At high NC concentration the aggregation of NC into ~1µm aggregates. This preliminary *operando* methodology shows how electrochemical impacts strategy in SECM can be used to reveal the NPs growth mechanism and could be extended to apprehend many other (oxide) NP electrosynthesis.

5 Acknowledgments

We thank the CNRS, and the Emergence call from the Université de Paris within the Investissement d'Avenir program under reference ANR-18-IDEX-0001 for financial support.

6 References

[1] R. Medhi, M.D. Marquez, T.R. Lee, Visible-Light-Active Doped Metal Oxide Nanoparticles: Review of their Synthesis, Properties, and Applications, ACS Applied

Nano Materials. 3 (2020) 6156–6185. https://doi.org/10.1021/acsanm.0c01035.

[2] J. Zhu, L. Hu, P. Zhao, L.Y.S. Lee, K.-Y. Wong, Recent Advances in Electrocatalytic Hydrogen Evolution Using Nanoparticles, Chemical Reviews. 120 (2020) 851–918. https://doi.org/10.1021/acs.chemrev.9b00248.

[3] S. Mourdikoudis, L.M. Liz-Marzán, Oleylamine in Nanoparticle Synthesis, Chemistry of Materials. 25 (2013) 1465–1476. https://doi.org/10.1021/cm4000476.

[4] A. V Nikam, B.L. V Prasad, A.A. Kulkarni, Wet chemical synthesis of metal oxide nanoparticles: a review, CrystEngComm. 20 (2018) 5091–5107. https://doi.org/10.1039/C8CE00487K.

[5] M. Izzi, M.C. Sportelli, N. Ditaranto, R.A. Picca, M. Innocenti, L. Sabbatini, N. Cioffi, Pros and Cons of Sacrificial Anode Electrolysis for the Preparation of Transition Metal Colloids: A Review, ChemElectroChem. 7 (2020) 386–394. https://doi.org/10.1002/celc.201901837.

[6] Q.-T. Pham, B.T. Huy, Y.-I. Lee, New highly efficient electrochemical synthesis of dispersed Ag2O particles in the vicinity of the cathode with controllable size and shape, J. Mater. Chem. C. 3 (2015) 7720–7726. https://doi.org/10.1039/C5TC01274K.

[7] Y.E. Jeun, B. Baek, M.W. Lee, H.S. Ahn, Surfactant-free electrochemical synthesis of metallic nanoparticles via stochastic collisions of aqueous nanodroplet reactors, Chem. Commun. 54 (2018) 10052–10055. https://doi.org/10.1039/C8CC05760E.

[8] M.W. Glasscott, A.D. Pendergast, S. Goines, A.R. Bishop, A.T. Hoang, C. Renault, J.E. Dick, Electrosynthesis of high-entropy metallic glass nanoparticles for designer, multi-functional electrocatalysis, Nature Communications. 10 (2019) 2650. https://doi.org/10.1038/s41467-019-10303-z.

[9] P.D. Morris, I.J. McPherson, M.A. Edwards, R.J. Kashtiban, R.I. Walton, P.R. Unwin, Electric Field-Controlled Synthesis and Characterisation of Single Metal–Organic-Framework (MOF) Nanoparticles, Angewandte Chemie International Edition. n/a (n.d.). https://doi.org/10.1002/anie.202007146.

[10] P.D. Morris, I.J. McPherson, G.N. Meloni, P.R. Unwin, Nanoscale kinetics of amorphous calcium carbonate precipitation in H2O and D2O, Physical Chemistry Chemical Physics : PCCP. 22 (2020) 22107–22115. https://doi.org/10.1039/d0cp03032e.

[11] Q. Wang, J.H. Bae, A.B. Nepomnyashchii, R. Jia, S. Zhang, M. V Mirkin, Light-Controlled Nanoparticle Collision Experiments, The Journal of Physical Chemistry Letters. 11 (2020) 2972–2976. https://doi.org/10.1021/acs.jpclett.0c00585.

[12] D.A. Robinson, H.S. White, Electrochemical Synthesis of Individual Core@Shell and Hollow Ag/Ag2S Nanoparticles, Nano Letters. 19 (2019) 5612–5619. https://doi.org/10.1021/acs.nanolett.9b02144.

[13] X. Xiao, A.J. Bard, Observing Single Nanoparticle Collisions at an Ultramicroelectrode by Electrocatalytic Amplification, Journal of the American Chemical Society. 129 (2007) 9610–9612. https://doi.org/10.1021/ja072344w.

[14] T.J. Stockmann, L. Angelé, V. Brasiliense, C. Combellas, F. Kanoufi, Platinum Nanoparticle Impacts at a Liquid|Liquid Interface, Angewandte Chemie International Edition. 56 (2017) 13493–13497. https://doi.org/10.1002/anie.201707589.

[15] B.M. Quinn, P.G. van't Hof, S.G. Lemay, Time-Resolved Electrochemical Detection of Discrete Adsorption Events, Journal of the American Chemical Society. 126 (2004) 8360–8361. https://doi.org/10.1021/ja0478577.

[16] Z. Deng, C. Renault, Detection of individual insulating entities by electrochemical blocking, Current Opinion in Electrochemistry. 25 (2021) 100619. https://doi.org/https://doi.org/10.1016/j.coelec.2020.08.001.

[17] H. Ma, J.-F. Chen, H.-F. Wang, P.-J. Hu, W. Ma, Y.-T. Long, Exploring dynamic interactions of single nanoparticles at interfaces for surface-confined electrochemical behavior and size measurement, Nature Communications. 11 (2020) 2307. https://doi.org/10.1038/s41467-020-16149-0.

[18] J.-F. Lemineur, J.-M. Noël, C. Combellas, F. Kanoufi, Revealing the sub-50 ms electrochemical conversion of silver halide nanocolloids by stochastic electrochemistry and optical microscopy, Nanoscale. 12 (2020) 15128–15136. https://doi.org/10.1039/D0NR03799K.

[19] Y.-G. Zhou, N. V Rees, R.G. Compton, The Electrochemical Detection and Characterization of Silver Nanoparticles in Aqueous Solution, Angewandte Chemie International Edition. 50 (2011) 4219–4221. https://doi.org/10.1002/anie.201100885.

[20] A.J. Bard, M. V. Mirkin, Scanning Electrochemical Microscopy, 2nd Editio, CRC Press, Boca Raton, 2012. https://doi.org/10.1201/b11850.

[21] K. McKelvey, D.A. Robinson, N.J. Vitti, M.A. Edwards, H.S. White, Single Ag nanoparticle collisions within a dual-electrode micro-gap cell, Faraday Discuss. 210 (2018) 189–200. https://doi.org/10.1039/C8FD00014J.

[22] B.J. Murray, Q. Li, J.T. Newberg, E.J. Menke, J.C. Hemminger, R.M. Penner, Shape- and size-selective electrochemical synthesis of dispersed silver(l) oxide colloids, Nano Letters. 5 (2005) 2319–2324. https://doi.org/10.1021/nl051834o.

[23] S. Boopathi, S. Gopinath, T. Boopathi, V. Balamurugan, R. Rajeshkumar, M. Sundararaman, Characterization and Antimicrobial Properties of Silver and Silver Oxide Nanoparticles Synthesized by Cell-Free Extract of a Mangrove-Associated Pseudomonas aeruginosa M6 Using Two Different Thermal Treatments, Industrial & Engineering Chemistry Research. 51 (2012) 5976–5985. https://doi.org/10.1021/ie3001869.

[24] J. Pan, Y. Sun, Z. Wang, P. Wan, X. Liu, M. Fan, Nano silver oxide (AgO) as a super high charge/discharge rate cathode material for rechargeable alkaline batteries, J. Mater. Chem. 17 (2007) 4820–4825. https://doi.org/10.1039/B711373K.

[25] W. Jiang, X. Wang, Z. Wu, X. Yue, S. Yuan, H. Lu, B. Liang, Silver Oxide as Superb and Stable Photocatalyst under Visible and Near-Infrared Light Irradiation and Its Photocatalytic Mechanism, Industrial & Engineering Chemistry Research. 54 (2015) 832–841. https://doi.org/10.1021/ie503241k.

[26] Z. Jusys, R.J. Behm, The Effect of Anions and pH on the Activity and Selectivity of an Annealed Polycrystalline Au Film Electrode in the Oxygen Reduction Reaction-Revisited, ChemPhysChem. 20 (2019) 3276–3288. https://doi.org/10.1002/cphc.201900960.

[27] J.-F. Lemineur, J.-M. Noël, A. Courty, D. Ausserré, C. Combellas, F. Kanoufi, In Situ Optical Monitoring of the Electrochemical Conversion of Dielectric Nanoparticles: From Multistep Charge Injection to Nanoparticle Motion, Journal of the American Chemical Society. 142 (2020) 7937–7946. https://doi.org/10.1021/jacs.0c02071.

[28] T.R. Bartlett, S. V Sokolov, R.G. Compton, Electrochemical Nanoparticle Sizing Via Nano-Impacts: How Large a Nanoparticle Can be Measured?, ChemistryOpen. 4 (2015) 600–605. https://doi.org/https://doi.org/10.1002/open.201500061.

[29] R.R.M. Johnston, M. Spiro, Diffusion coefficients of the silver ion and the disulfitosilver (I) ion by the rotating disk method, The Journal of Physical Chemistry. 71 (1967) 3784–3790. https://doi.org/10.1021/j100871a011.

[30] W. Xing, M. Yin, Q. Lv, Y. Hu, C. Liu, J. Zhang, 1 - Oxygen Solubility, Diffusion Coefficient, and Solution Viscosity, in: W. Xing, G. Yin, J.B.T.-R.E.M. and O.R.E. Zhang (Eds.), Elsevier, Amsterdam, 2014: pp. 1–31. https://doi.org/https://doi.org/10.1016/B978-0-444-63278-4.00001-X.

[31] F.C. Sauls, A Simple Determination of the Ag2O Solubility Product by Potentiometric Determinations of Both Ag+1 and OH–1, Journal of Chemical Education. 90 (2013) 1212–1214. https://doi.org/10.1021/ed300586g.

[32] J.Y. Choi, T. Lee, Y. Cheng, Y. Cohen, Observed Crystallization Induction Time in Seeded Gypsum Crystallization, Industrial & Engineering Chemistry Research. 58 (2019) 23359–23365. https://doi.org/10.1021/acs.iecr.9b06050.

[33] M.A. Mousa, M.A. Ahmed, Crystallization kinetics of amorphous Ge20Se5Te75, Thermochimica Acta. 140 (1989) 155–160. https://doi.org/10.1016/0040-6031(89)87294-6.

[34] J.-M. Noël, M. Miranda Vieira, V. Brasiliense, J.-F. Lemineur, C. Combellas, F. Kanoufi, Effect of the driving force on nanoparticles growth and shape: an opto-electrochemical study, Nanoscale. 12 (2020) 3227–3235. https://doi.org/10.1039/C9NR09419A.

[35] V. Brasiliense, J.-M. Noël, K. Wonner, K. Tschulik, C. Combellas, F. Kanoufi, Single Nanoparticle Growth from Nanoparticle Tracking Analysis: From Monte Carlo Simulations to Nanoparticle Electrogeneration, ChemElectroChem. 5 (2018) 3036–3043. https://doi.org/10.1002/celc.201800742.